CrossMark

Soft X-Ray-induced Dimerization of Methane

S. Reinwardt[1] , I. Baev[1] , P. Cieslik[1] , K. Baev[2] , T. Buhr[3] , A. Perry-Sassmannshausen[3] , S. Schippers[3] , A. Müller[3] ,
F. Trinter[4,5] , J. Viefhaus[6] , and M. Martins[1]

[1] Institut für Experimentalphysik, Universität Hamburg, Luruper Chaussee 149, D-22761 Hamburg, Germany; michael.martins@uni-hamburg.de
[2] Deutsches Elektronen-Synchrotron (DESY), Notkestraße 85, D-22607 Hamburg, Germany
[3] I. Physikalisches Institut, Justus-Liebig-Universität Gießen, Heinrich-Buff-Ring 16, D-35392 Giessen, Germany
[4] Institut für Kernphysik, Goethe-Universität Frankfurt, Max-von-Laue-Straße 1, D-60438 Frankfurt am Main, Germany
[5] Molecular Physics, Fritz-Haber-Institut der Max-Planck-Gesellschaft, Faradayweg 4-6, D-14195 Berlin, Germany
[6] Helmholtz-Zentrum Berlin für Materialien und Energie, Hahn-Meitner-Platz 1, D-14109 Berlin, Germany

Abstract

Carbon 1s excitation of methane, CH_4, has been studied in the gas phase using the ion trap integrated with the photon–ion instrument at PETRA III/DESY and soft X-rays from the beamline P04. The created photoions are stored within the ion trap so that in further steps the photoions can undergo reactions with neutral methane molecules. The ionic photoproducts as well as reaction products created thereby are mass-over-charge analyzed by an ion time-of-flight spectrometer. Besides the photoions, product ions with up to three carbon atoms are found. In contrast to experiments using vacuum ultraviolet radiation, especially highly reactive product ions with a small number of hydrogen atoms such as $C_2H_2^+$ and $C_2H_3^+$ are found, which are important precursors for larger hydrocarbons such as C_6H_6. Possible production routes of the product ions are analyzed on the basis of a model that considers the probabilities for photofragmentation and the first subsequent chemical reaction step. The model indicates that the high degree of fragmentation by photons with energies around 280 eV is favoring these products. The results of the measurements show that the products like $C_2H_2^+$ and $C_2H_3^+$ can be generated by a single collision of the ionization product with neutral methane. The results suggest that soft X-rays might be important for chemical reactions in planetary atmospheres, which has usually not been taken into account. However, due to the high degree of fragmentation and large cross sections involved, they can have a large influence even when the corresponding photon flux is rather small.

Unified Astronomy Thesaurus concepts: Planetary atmospheres (1244)

1. Introduction

In the last decades, a large variety of molecules and molecular ions has been found in space and in the atmospheres of celestial bodies (McGuire 2022). Among them are hydrocarbons and organic molecules, which must result from complex chemical processes. Of particular interest and well-studied is the atmosphere of the Saturn moon Titan, which mainly consists of methane, CH_4, and nitrogen, N_2 (Kuiper 1944; Hörst 2017). However, also hydrocarbons such as benzene c-C_6H_6 (Waite et al. 2007; Vuitton et al. 2008b) or cyclopropenylidene c-C_3H_2 (Nixon et al. 2020) are found. The formation of such complex molecules in the atmosphere of Titan or in other environments, such as the interstellar medium, is the topic of various studies (Herbst & Klemperer 1973; Fox & Yelle 1997; Keller et al. 1998; Banaszkiewicz 2000; Waite et al. 2007; Oscar Martinez et al. 2008; Tielens 2008; Vuitton et al. 2008a, 2008b; Thissen et al. 2009; Habart et al. 2010; Berne & Tielens 2011; Peng et al. 2013; Hörst 2017; Meyer & Wester 2017; Bastian et al. 2019; Bourgalais et al. 2019). A possible mechanism is their formation starting from smaller molecules such as CH_4 by chain growth reactions, in which carbon atoms or CH_n groups are added to a precursor step by step (Waite et al. 2007; Vuitton et al. 2008b).

The initialization step of a chain growth reaction might be triggered by a chemical breakup of a starter molecule into one or more reactive species or by generating a reactive excited state, for example, by selective excitation with photons. In atmospheres (Kulmala 2003; Holmes 2007) or in the interstellar medium (Martinez et al. 2008; Berne & Tielens 2011), starlight plays the primary role in the activation of growth reactions.

Chain growth reactions occur easily if functional groups or double bonds are present in a molecule. Such bonds are found for example between pure ethylene and carbon anions (Bastian et al. 2019). As methane is lacking such reactive sites, it is rather inert and does not react easily in growth reactions. By the absorption of a photon, excited states can be created or fragmentation can occur including the production of reactive ions. Alternative methods like plasma polymerization can be used (Sharma & Yasuda 1989) to activate methane. For example, polycyclic aromatic hydrocarbons can be generated from a methane gas flame (Senkan & Castaldi 1996).

Various experiments have been carried out to understand the formation of carbon compounds in celestial atmospheres. To simulate the Titan atmosphere, a nitrogen–methane mixture was excited with vacuum ultraviolet (VUV) radiation, and carbon addition reactions were observed (Thissen et al. 2009; Peng et al. 2013; Bourgalais et al. 2019). However, important precursors and highly reactive species observed in the ionosphere of Titan, such as C_2H_2, C_2H_3, or the corresponding cations (Thissen et al. 2009), could not be found in the VUV experiments and thus cannot significantly contribute to the formation of larger molecules as observed in Titan's

atmosphere. In the VUV study by Bourgalais et al. (2019), no C_2H_2 was found, while Peng et al. (2013) might have observed C_2H_2, but due to the rather low mass resolution of their experiment the result is ambiguous.

An important quantity to start the growth reaction and produce a decent number of larger molecules is the number of available photons. The photon flux of VUV radiation from the Sun around 50 eV photon energy (25 nm) is of the order of $1 \times 10^9 \, \text{ph}^2 \, \text{cm}^{-1} \, \text{s}^{-1} \, \text{nm}^{-1}$ (Woods et al. 2000) corresponding to $5 \times 10^7 \, \text{ph}^2 \, \text{cm}^{-1} \, \text{s}^{-1} \, \text{eV}^{-1}$. The Sun also emits soft X-rays originating from its very hot corona (Rusov et al. 2021) and Saturn itself emits X-rays as well (Bhardwaj et al. 2005; Branduardi-Raymont et al. 2010). The soft X-ray photon flux is around $1 \times 10^5 \, \text{ph}^2 \, \text{cm}^{-1} \, \text{s}^{-1} \, \text{eV}^{-1}$ at 500 eV (Caspi et al. 2015) and is 2-3 orders of magnitudes lower than the VUV flux. Therefore, the influence of soft X-rays on the creation of larger molecules has usually been ignored and only a few soft X-ray measurements have been performed (Young 2021). Also in theoretical models for the creation of small hydrocarbon molecules (Fox & Yelle 1997; Keller et al. 1998; Hollenbach & Tielens 1999; Banaszkiewicz 2000), soft X-rays in the energy range above 200 eV are usually neglected and only a few models (Hollenbach & Tielens 1999) include them. However, soft X-ray excitation at or above the C 1s edge can produce very reactive ions due to the higher level of fragmentation as compared to valence excitations. This stronger fragmentation can be seen when comparing the VUV and soft X-ray absorption by methane (Wolff et al. 2012). Following a C 1s excitation, the number of smaller fragmentation products with few H atoms is increased by 1–2 orders of magnitude. By resonant excitations the photoionization cross section is enhanced and the photon–matter interaction probability is strongly increased resulting in an even larger amount of smaller photofragments.

The above discussion suggests that the influence of soft X-rays on the production of hydrocarbons in planetary atmospheres or in the interstellar medium requires further investigation. In order to achieve this, a tunable soft X-ray light source with high resolving power and high photon flux, in combination with a well-defined reaction volume are needed. By the combination of beamline P04 and our ion-trap setup, it is possible to simulate the conditions present, e.g., in Titan's thermosphere or ionosphere, where small hydrocarbon systems have been observed in recent studies (Vuitton et al. 2008a; Nixon et al. 2020). With the experiment presented here, the formation of complex hydrocarbons in planetary atmospheres and in the interstellar medium is elucidated. We chose pure methane as the precursor molecule for this study, because this reduces the number of possible reactions relative to mixtures of nitrogen and methane significantly. Performing time-of-flight mass spectrometry enables studies of chemical ion compositions of molecular ions in the reaction volume and thus facilitates the direct assignment of each observed ion mass to a specific reaction path. In this paper, we investigate specific changes in the chemical ion composition by addressing different C 1s resonant excitations of methane individually. We focus here especially on the first reaction step and how it depends on the photon energy.

2. Experimental Setup

Reactions of methane photoions and methane molecules have been investigated using the radio-frequency ion trap of the
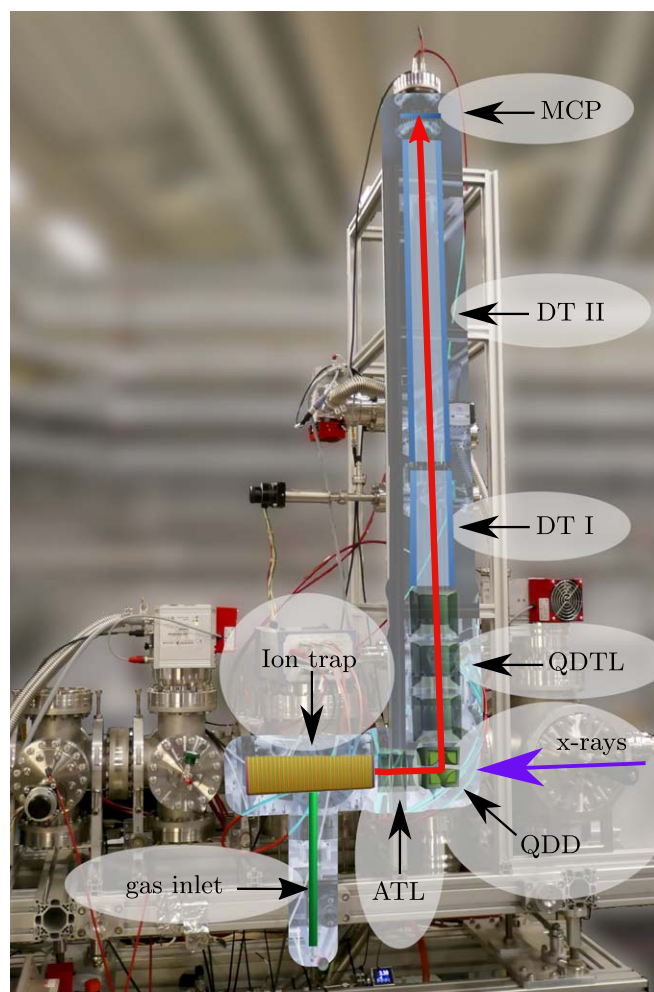

Figure 1. Overview of the ion trap at the PIPE setup. The soft X-ray beam enters from the right. The ions leave the ion trap to the right via the after-trap lens (ATL) system. The extracted ions are deflected upward by the electrostatic quadrupole deflector (QDD) and focused with a quadrupole-triplet lens (QDTL) into the drift tubes DT I and DT II. The ions are detected using a Chevron microchannel-plate (MCP) stack. The red line indicates the ions' flight path.

permanent photon–ion spectrometer setup (PIPE) at the synchrotron light source PETRA III. The ion trap is a hybrid structure and can be operated as either a ring electrode or a segmented 16-pole trap (Reinwardt et al. 2023). This ion trap is used to study the production of larger molecules from X-ray-irradiated methane. Methane is injected into the trap via a metering valve. A methane bottle quoted to contain CH_4 at a purity level of 99,995%[7] was connected to the experiment and used as received. In the high-vacuum chamber, a methane pressure of 1.6×10^{-3} Pa was measured with an ionization vacuum gauge. The relative sensitivity of the pressure gauge was corrected for methane with a factor of 1.62 (Bartmess & Georgiadis 1983). This pressure corresponds to the conditions in Titan's ionosphere (Thissen et al. 2009). In the ion trap, the neutral methane molecules are continuously illuminated by the incoming soft X-rays and can be ionized. The resulting photoions are captured by the radio-frequency potential of the ion trap operated at room temperature. That is, the
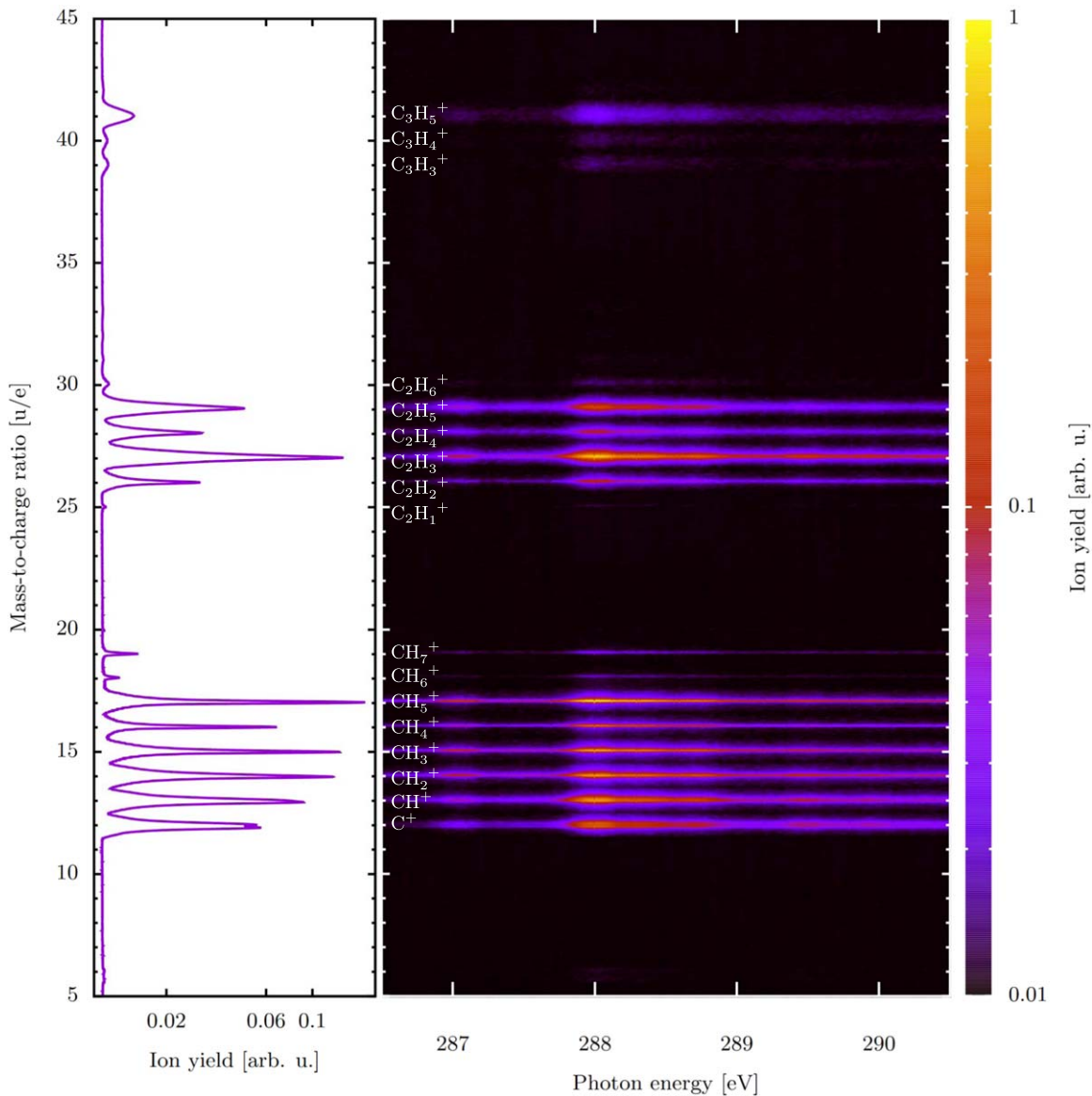
Figure 2. NEXAFS (near edge X-ray absorption fine structure) ion time-of-flight map of methane at the C 1s edge measured after a certain trapping time of 3 ms. In addition to the primary CH_x^+ photofragment series, secondary heavier molecular ions are clearly observed which can only be the products of additional reactions of primary fragments with neutral methane molecules. These products are identified as $C_2H_x^+$ and $C_3H_x^+$ ions which incorporate two or three carbon atoms.

experimental temperature is above the typical temperatures of the Titan ionosphere of 150 K (Fulchignoni et al. 2005). The ion trap was operated with a radio frequency of 3 MHz and a radio-frequency amplitude of 20 V. To measure the mass-over-charge ratios of the trapped ions, time-of-flight spectra were recorded with a repetition rate of 295 Hz. The ions were collected over a period of 3 ms and then extracted from the trap and directed to the time-of-flight spectrometer. The ions' flight path through the ion-trap setup is shown in Figure 1. A detailed description of the trap setup has been given by Reinwardt et al. (2023).

The soft X-ray beamline P04 was operated with a 400 lines/mm grating and an exit-slit width of 100 μm giving an energy resolution of 0.2 eV. In this operation mode of the beamline, the photon flux is 6.7×10^{11} s^{-1} at a photon energy of 285.6 eV. The photon energy has been calibrated to the known resonances of methane (Schirmer et al. 1993; Urquhart & Gillies 2005). All recorded time-of-flight spectra were normalized to the photon flux measured by a calibrated photodiode. The methane pressure

was kept constant during the measurement. Photon-energy-dependent time-of-flight spectra were recorded around the carbon K-edge from 285 eV up to 292 eV. To measure a high-resolution reference spectrum for methane, the beamline was operated with a 1200 lines/mm grating and an exit-slit width of 100 μm. With this configuration, an energy resolution of 30 meV was obtained.

3. Results

The right panel of Figure 2 shows a 2D intensity map of the ion yield as a function of the mass-over-charge ratio and the photon energy. The time-of-flight mass spectrum in the left panel was obtained by integrating the measured ion yields in the intensity map along the photon-energy axis. The photo-fragments CH_x^+ with different numbers x of hydrogen atoms ($x = 0–4$) are well separated. In addition to singly photoionized methane and its fragments CH_x^+, the map in Figure 2 shows ions with a mass that corresponds to that of supermethanium
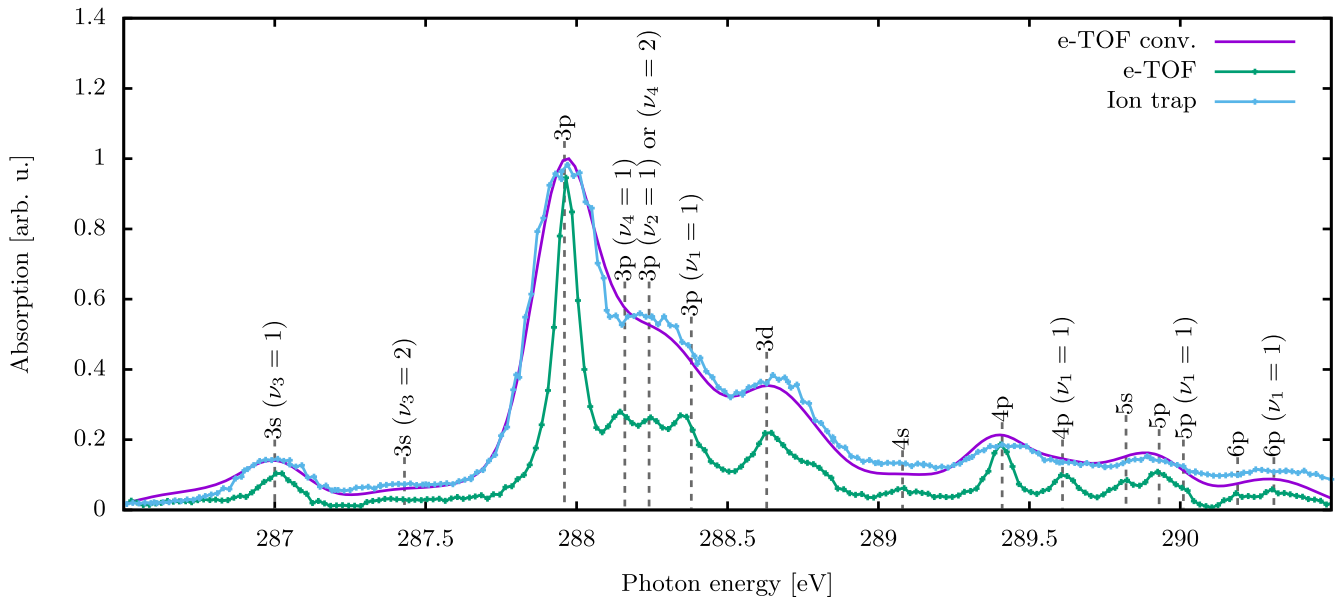
Figure 3. The photoabsorption spectrum of methane measured with the ion trap compared to an electron-yield spectrum obtained with an electron time-of-flight (e-TOF) spectrometer. The latter spectrum was recorded by 16 identical time-of-flight electron detectors, which are housed in the diagnostic unit of the soft X-ray beamline P04 (Buck et al. 2019). For comparison of the e-TOF result with the lower-resolution ion-trap data, the energy resolution was adapted to the experimental resolution by convolution with a 0.2 eV FWHM Gaussian function.

ions, i.e., CH_x^+ ions with $x = 5–7$ and hydrocarbon ions $C_nH_x^+$ ($n = 2$, 3) with two or three carbon atoms. At the current experimental conditions and sensitivity reference time-of-flight spectra recorded for neon and xenon do not show any higher masses.

Photon-energy spectra for the individual fragments can be obtained from horizontal slices of the 2D map shown in Figure 2. In Figure 3, the C 1s near edge X-ray absorption fine structure (NEXAFS) spectrum, measured with the ion-trap setup is depicted. This NEXAFS spectrum is obtained by summing up the ion yields of the different CH_x^+ ($x = 0–4$) photofragmentation channels.

As a reference, a C 1s NEXAFS spectrum of CH_4 has been recorded by measuring the total electron yield using electron time-of-flight (TOF) spectrometers of a beam-diagnostics unit for beamline P04 (Buck et al. 2019). The photon-energy calibration was performed using the C $1s \rightarrow 3p$ transition in neutral methane at 287.96 eV (Urquhart & Gillies 2005). The ion-trap and electron-TOF spectra show a good agreement. Excitations into 3s, 3p, and 3d orbitals are clearly visible. The vibrational states characterized by quantum numbers ν and their energies are listed in Table 1. It can be assumed that the methane is in the vibronic ground state before the excitation. If also the excited level is in its vibronic ground state, the vibrational quantum number is omitted in the notation for the sake of readability. The usually dipole-forbidden $1s \rightarrow 3s$ transition is allowed due to the additional $\nu_3 = 1$ vibrational excitation of the t_2 symmetry (Bagus et al. 1973). The next peak represents the $1s \rightarrow 3p$ transition and exhibits a shoulder due to the vibrational excitations ($\nu_4 = 1$) and ($\nu_1 = 1$). It is followed by the $1s \rightarrow 3d$ transition, which is in agreement with the measurement by Urquhart & Gillies (2005). The $1s \rightarrow 3p$ ($\nu_4 = 2$) feature between the vibrational excitations ($\nu_4 = 1$) and ($\nu_1 = 1$) was not resolved in the experiment by Urquhart & Gillies (2005), but found in the experiment of Schirmer et al. (1993).

Table 1
Vibration Energies of the Different Vibrational States of Methane

Type	Notation	Exp.	Theo.
Symmetric stretch	ν_1	0.38(1) eV	0.36 eV
Bend	ν_2	0.28(1) eV	0.20 eV
Asymmetric stretch	ν_3	0.43(6) eV	0.38 eV
Bend	ν_4	0.18(1) eV	0.16 eV

Notes. The Herzberg notation is used. The theoretical values were taken from a publication by Lemus & Frank (1994). The experimental values were determined using Fano–Voigt fits on the curve "e-TOF" in Figure 3.

As the present spectra obtained with the trap were recorded with a photon-energy spread of 0.2 eV, this vibrational fine structure is not resolved and only a shoulder is visible. The weaker $1s \rightarrow 4p$ and $1s \rightarrow 5s$ resonances are observed but the $1s \rightarrow 5s$, $1s \rightarrow 5p$, and $1s \rightarrow 5d$ resonances cannot be separated energetically. Therefore, these resonances are summarized here as 5ℓ in the following discussion. A separation of the $1s \rightarrow 6p$ resonance and the $1s \rightarrow 6p$ ($\nu_1 = 1$) resonance was also not possible. Those resonances are summarized as 6ℓ.

The ion yields for the individual photofragment channels CH_x^+ ($x = 0–4$) are shown in Figure 4(a). Strong variations are found in these photon-energy-dependent yields for the different excitation processes. Upon a $1s \rightarrow 3s$ ($\nu_3 = 1$) excitation, the CH_3^+ channel shows the largest ion yield. For the $1s \rightarrow 3p$ excitation the CH^+ channel is by far the strongest. Upon this excitation, photofragmentation is clearly preferred while the CH_4^+ channel is the weakest at all energies.

In Figure 4(b), the photon-energy dependence of the ion yields for the hydrogen-addition channels CH_x^+ ($x = 5–7$) is depicted. As these ions are created subsequent to the excitation of neutral methane, they show a resonance structure similar to that of methane photoabsorption. In addition to the CH_5^+ ions, the significantly weaker signatures of supermethanium ions
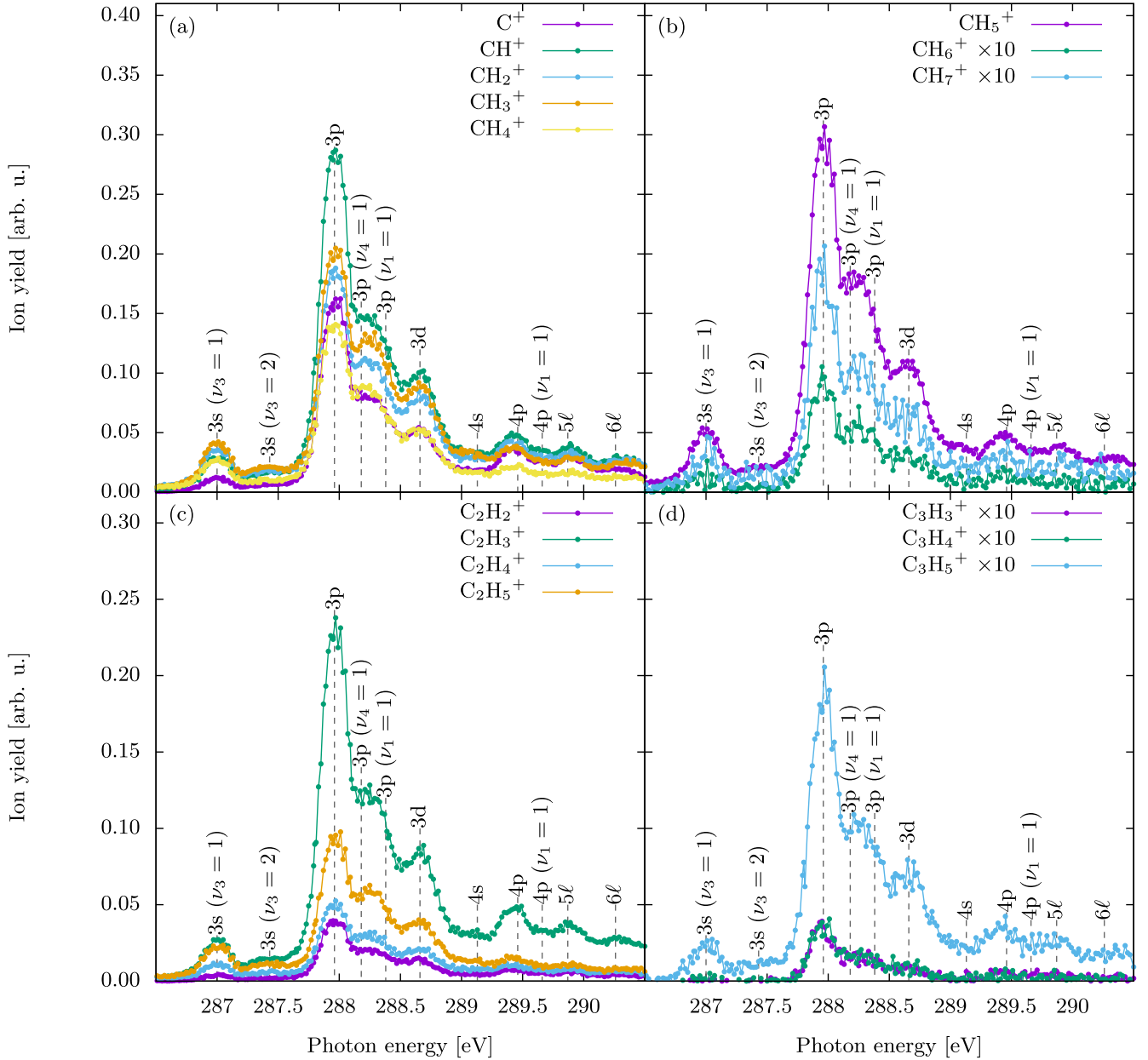
Figure 4. (a) Measured relative cross sections (product-ion yields) for photoionization and fragmentation of methane at the C 1s edge. Every photoabsorption product in this trap experiment can react with neutral methane. (b) Photon-energy dependencies of hydrogen-addition reaction channels. Note that the CH_6^+ and CH_7^+ yields have been multiplied by a factor of 10. (c) Photon-energy dependencies of dimerization channels of methane. Channels shown in (b) and (c) can only occur when ionic photoabsorption products, which are shown in (a), collide with at least one neutral methane molecule while stored in the trap. (d) Photon-energy dependencies of the trimerization of methane. These reaction products can only be formed by at least two methane-addition steps. Note that the yields in panel (d) have been multiplied by a factor of 10.

CH_6^+ and CH_7^+ are found. The CH_7^+ ions have already been observed by Gerlich 2005 in ion collision experiments.

Figures 4(c) and (d) show the photon-energy dependences of the ion yields for the reaction products with two and three carbon atoms, respectively. Among the reaction products, $C_2H_3^+$ is by far the strongest dimerization product channel. The second strongest channel is $C_2H_5^+$. The strongest product channel with three carbon atoms is $C_3H_5^+$, whose yield is about one order of magnitude smaller than that of $C_2H_3^+$.

4. Discussion

In the following, we will discuss mechanisms to produce the observed photofragments and heavier product ions based on

chain growth reactions. In the initialization step I of a possible reaction chain, a C 1s core electron in neutral methane is resonantly excited by a soft X-ray photon to one of the unoccupied molecular levels identified in Figure 3. This excitation is followed by an Auger decay, which ionizes the neutral molecule. Subsequent to the ionization, there is a possibility for a breakup reaction of the charged methane molecule, which produces among others C^+, CH^+, CH_2^+, or CH_3^+ fragments. The CH_4^+ photoabsorption products are trapped with the typical thermal energy around 38 meV of the neutral methane molecules. The fragment ions can have higher kinetic energies due to the photodissociation process. Following a valence excitation, the total kinetic energy release

Table 2
Estimated Kinetic Energies of the Different CH_n^+ Photofragment Ions (E_{KER}) Due to the Partial Kinetic Energy Release

fragment ion	E_{KER}	ref. E_{KER}	E_{radial}
$C_3H_5^+$	⋯	⋯	0.3 eV
$C_2H_3^+$	⋯	⋯	0.2 eV
CH_4^+	⋯	⋯	0.1 eV
CH_3^+	0.1 eV	0.02 eV	0.09 eV
CH_2^+	0.2 eV	0.20 eV	0.08 eV
CH^+	0.3 eV	0.24 eV	0.07 eV
C^+	0.4 eV	0.26 eV	0.07 eV

Note. The reference values (ref. E_{KER}) are taken from Wei et al. (2013). In addition, the maximum radial energy (E_{radial}) calculated by Equation 1 in the present ion trap is listed.

(KER) is around 1.5 eV for all fragments (Heck et al. 1996). This total KER will be shared between the fragments. Due to the large mass of CH_n^+ as compared to H or H_2, the partial KER of the CH_n^+ fragments is rather small. In Table 2, the partial KER of the CH_n^+ fragment ions and the corresponding maximum radial energy E_{radial} for an adiabatic trapping of the ions are shown. This radial energy can be obtained from Gerlich's theory (see Equation (24) of Gerlich 1992):

$$E_{radial} = \left(\frac{\eta \pi f r_0 \hat{r}}{2(n-1)} \right)^2 m_{ion},\qquad(1)$$

where f is the frequency of the radio-frequency potential. η is the stability parameter that must be below 0.3 for stable trapping. $r_0 = 5$ mm is the radius of the ion trap and n is the number of rod pairs. $\hat{r}$ is the reduced radius in the order of 0.72 for the C^+ ion and increasing to $\cong 0.9$ for product ions with three C atoms. These numbers can be estimated from the adiabatic parameter (Mikosch et al. 2008). By comparing the energies in Table 2, it can be seen that E_{radial} is similar to E_{KER} for the hydrogen-rich fragments, and the efficiency to trap ions with a small mass (C^+, CH^+) resulting from a strong fragmentation is reduced. Here, it must be pointed out that the energies given for E_{KER} are associated with a two-particle breakup. For a many-particle breakup with a total charge of $+e$ for all products, the given KER value is an upper limit as an unknown amount of KER is distributed across the neutral hydrogen fragments. This estimation for the fragments is consistent with the experimental KER values measured by electron-impact ionization (Wei et al. 2013). Since the molecules are randomly oriented, the released kinetic energy is partly released in the radial direction and partly in the axial direction of the ion trap. By distributing the kinetic energy in the radial and axial directions for a portion of molecular orientations, the radial kinetic energy of the fragmented ions is below E_{radial}, and adiabatic trapping of the ions is achieved.

At temperatures of 293 K and below, one can safely assume that the methane is in the vibronic ground state. The decay of the photoexcited state can lead to a kinetic energy release, which leads to an increase in the kinetic energy of the ionic fragments and a reduction in the probability of trapping those fragments. The trapped photoions can collide with neutral methane molecules. This collision can induce step II, the starting reaction for subsequent step-by-step growth reactions.

In the case of a Coulomb explosion following the C 1s excitation, the kinetic energy of the ions increases by a few electron volts. A Coulomb explosion will be possible only in the case of a double Auger process, as the intermediate methane molecule must be at least doubly charged. Photo-ionization experiments on atomic C^+ ions show that the double-ionization probability is of the order of 3% of the single-ionization probability (Müller et al. 2018). Therefore, the Coulomb explosion is rather unlikely and will not be considered further. Also, reactive ion–ion collision processes are expected to have a low probability due to the Coulomb repulsion of the ions and because of the low density of ions compared to neutral molecules. Hence, ion–ion collisions will not be taken into account.

The formation probability for a given reaction product depends on the electronic and vibrational state of the photoion as well as on the gas pressure. The $C_nH_{k+4-n}^+ (n = 2, 3)$ channels comprise ions that result from a chemical reaction of the trapped ionic photofragments with the neutral methane molecules in the trap. The associated reactions may be described by

$$CH_4 \xrightarrow[(4-k)H]{h\nu} [CH_k^+]^{\neq} \xrightarrow[nH]{CH_4} C_2H_{k+4-n}^+.\qquad(R1)$$
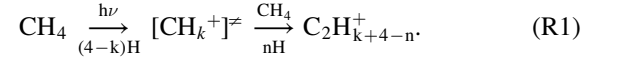
The $\neq$ in the equation stands for a transition state. In a second step, the $C_2H_{k+4-n}^+$ ion resulting from the reaction might react with a second neutral methane molecule:

$$C_2H_{k+4-n}^+ \xrightarrow[mH]{CH_4} C_3H_{k+8-n-m}^+.\qquad(R2)$$
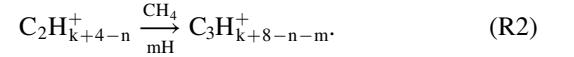
The reaction in Equation R2 is the second growth step and more growth reactions can follow. With the progression of growth, the influence of the activating process decreases from step to step. Further parameters, such as the change in kinetic energy of the products during the growth process or the varying chemical reactivity will become more important and will dominate the further growth.

Here, we will focus on the influence of the photon energy in the first two steps in more detail. For an ion–neutral-molecule reaction, the probability of an impact is crucial, which can be estimated by the mean free path of the photoion. At a pressure of 1.6×10^{-3} Pa, the ideal gas law gives a particle density of 3.9×10^{11} cm^{-3}. From the polarizability of methane, which is 2.6×10^{-24} cm^3 (Gussoni et al. 1998), a Langevin constant (Langevin 1905; Gioumousis & Stevenson 1958) of 1.3×10^{-9} cm^{-3} s^{-1} can be calculated. The reaction rate and particle density result in a mean time between photoionization and reaction of 2 ms. Furthermore, the time between photoionization and reaction can also be estimated via the total reaction cross section. The total cross section for the reaction between a CH_4^+ ion and a neutral CH_4 molecule is 3.9 Gb (3.9×10^{-15} cm^{-2}) at room temperature (Wexler & Jesse 1962). In a simple classical model, the methane molecule can be represented as a sphere with a radius of 190 pm. Accordingly, the collision probability of two methane molecules is given by a cross section of $\sigma \approx 4.5 \times 10^{-15}$ cm^{-2}. The classical value is therefore close to the measured value of Wexler & Jesse (1962), and we can assume that every collision is a reactive collision. With a particle density of 3.9×10^{11} cm^{-3}, the mean free path of methane is $\cong 7$ m. The average thermal energy of the methane ions is 38 meV, which corresponds to a velocity of 677 ms^{-1}. With this velocity, a methane ion collides with a neutral methane molecule in an average time around 10 ms. The

Table 3
Areas of the Products for the Individual Resonances Determined from the Voigt Fits

Resonances	C^+	CH^+	CH_2^+	CH_3^+	CH_4^+	CH_5^+	CH_6^+	CH_7^+	$C_2H_2^+$	$C_2H_3^+$	$C_2H_4^+$	$C_2H_5^+$	$C_3H_5^+$
3 s ($\nu_3 = 1$)	2.6(4)	6.1(4)	7.2(3)	8.9(4)	6.2(3)	11.3(5)	0.3(1)	0.7(1)	0.9(1)	5.5(4)	2.2(1)	5.1(2)	0.5(1)
3 s ($\nu_3 = 2$)	0.3(6)	3.6(8)	3.1(5)	4.7(6)	1.9(5)	3.6(8)	0.1(1)	0.3(1)	0.5(2)	2.7(7)	1.3(2)	3.3(3)	0.3(1)
3p	44.1(5)	79.9(7)	49.8(4)	54.8(5)	39.3(4)	82.5(7)	2.5(1)	4.8(1)	10.9(1)	63.5(6)	13.5(1)	25.6(3)	5.2(1)
3p ($\nu_4 = 1$)	14.7(4)	26.5(5)	19.6(3)	23.5(4)	16.8(3)	33.8(5)	1.0(1)	1.8(1)	3.7(1)	22.3(4)	5.4(1)	11.2(2)	1.9(1)
3p ($\nu_3 = 1$)	8.2(4)	16.0(5)	9.5(3)	12.8(4)	7.4(3)	17.4(5)	0.6(1)	1.1(1)	2.2(1)	12.5(4)	2.6(1)	5.7(2)	1.1(1)
3 s ($\nu_3 = 1$)	15.3(5)	30.1(7)	22.3(5)	25.9(5)	15.8(4)	32.4(7)	0.9(1)	1.9(1)	4.2(1)	24.7(6)	5.9(1)	11.8(3)	2.2(1)
4 s	3.8(7)	7.2(9)	3.2(6)	5.6(6)	2.4(5)	7.6(8)	0.2(1)	0.4(1)	1.0(2)	5.9(8)	1.4(2)	3.0(3)	0.6(1)
4p	6.4(4)	7.2(5)	5.2(3)	4.1(4)	3.9(3)	6.5(5)	0.4(1)	0.4(1)	1.3(1)	7.3(4)	1.4(1)	2.0(2)	0.6(1)
4p ($\nu_1 = 1$)	3.0(4)	3.1(4)	1.3(3)	0.9(3)	0.8(3)	2.8(4)	0.1(1)	0.1(1)	0.5(1)	2.8(4)	0.4(1)	0.7(2)	0.2(1)
5ℓ	5.0(4)	4.8(5)	2.3(3)	1.7(4)	1.5(3)	4.7(5)	0.1(1)	0.3(1)	1.0(1)	4.6(4)	0.7(1)	1.1(2)	0.4(1)
6ℓ	2.2(4)	2.2(5)	0.4(3)	0.3(3)	0.3(3)	1.7(5)	0.0(1)	0.1(1)	0.4(1)	2.0(4)	0.3(1)	0.3(2)	0.2(1)

Notes. The values are given in 10^{-3} (arb. u.). The number in brackets indicates the error from the value.

fragment ions have an additional energy contribution from the kinetic energy release (see Table 2). The additional velocity of the CH^+ ion is around 2×10^3 ms^{-1}. Depending on the dissociation direction, this velocity can be decreased or increased by the thermal velocity. With this, the average collision time of the CH^+ ion and the neutral methane is in the range of 3–12 ms. Since the pressure was measured at the chamber wall, it can be assumed that the pressure in the ion trap was slightly higher and the mean time between photoionization and reaction in the real system was shorter. The two estimates show that in the experiment the typical collision time should be in the range of 2–12 ms. Hence, with the chosen trapping time of 3 ms, the performed experiments are in the single-collision regime.

This assumption is validated by the proportion of single- and double-collision reaction products. For example, the amount of the double-collision product $C_3H_5^+$ is 10 times lower as compared to the single-collision products, such as $C_2H_3^+$ (see Figure 4). The chosen pressure of 1.6×10^{-3} Pa and the 3 ms trapping time are ideal parameters, since mainly products resulting from only one reactive collision were observed. Only a small part of the single-collision products is lost through further reactions.

The very weak product channels $C_3H_3^+$ and $C_3H_4^+$ are also shown in Figure 4(d). A definitive statement about their formation cannot be made from the outlined data, however, the formation process should be similar to that of $C_3H_5^+$ and the most probable process is the formation from $C_2H_3^+$ and $C_2H_2^+$ by a H_2 or H elimination. In principle, $C_3H_3^+$ might be formed also from C_2H^+ as a possible precursor, but the C_2H^+ channel is very weak.

From Figures 2 and 4 it is obvious that the $C_2H_3^+$ ion is by far the strongest dimerization product channel. According to Equation R1, this channel must be formed by a reaction between a CH^+ ion and a neutral methane molecule, which is accompanied by the loss of two H atoms. The CH_3^+ ion is the second strongest photofragment channel as shown in Figure 4(a). According to Equation R1, this ion can produce $C_2H_5^+$. At the 1s → 3s ($\nu_3 = 1$) resonance, the CH_3^+ ion yield is larger than the CH^+ yield, which should in a simple approximation be valid also for the intensity ratio of the $C_2H_3^+$ and $C_2H_5^+$ products. Figure 4(c) illustrates that this is not the case. At the 1s → 3s ($\nu_3 = 1$) resonance, the $C_2H_3^+$ yield is larger than the $C_2H_5^+$ yield. This result shows that a reaction product ion does not necessarily have to be formed from a specific reactant ion. Only in this way is it possible that the $C_2H_3^+$ channel has almost the same intensity upon the 1s → 3s ($\nu_3 = 1$) excitation as that of CH^+. This results in various possible reaction pathways for the carbon addition products.

In contrast to VUV radiation, soft X-rays are able to excite carbon core electrons in methane, which results in stronger fragmentation (Wolff et al. 2012) and produces ions with an increased reactivity. This photofragmentation behavior of the molecule plays a decisive role in the subsequent reaction.

In order to understand the formation of ions in more detail, the ion composition was analyzed for the different resonances listed in Figure 5 and Table 3. The resonance widths, heights, and energy positions were determined by Voigt fits and the C 1s ionization edge was fitted with an arc tangent function. The areas of the resonances in Table 3 were determined by means of the Voigt fits and are depicted in Figure 5(a). Figure 5(b) shows the relative compositions of the product ions, which are obtained from the areas of the Voigt functions normalized to the sum of the other product ions of each resonance. This sum corresponds to a summation of a row in Table 3. In this way, the yield of the photoproducts for the different resonances can be directly compared. For the very weak $C_3H_3^+$ and $C_3H_4^+$ channels, the analysis shown in Figure 5 could not be performed. Figure 5 clarifies that the excitation into the 4ℓ, 5ℓ, and 6ℓ Rydberg states results in a higher degree of fragmentation. With increasing resonance energy, the proportion of C^+ and CH^+ increases. In the case of excitations into 3ℓ valence states, there is less fragmentation with a larger yield of CH_2^+, CH_3^+, and CH_4^+ photofragments. In particular, the vibrationally excited states ν_1 (symmetric stretch) and ν_4 (bend) show less fragmentation. Upon these excitations, energy can be dissipated into vibrations of the methane molecule and the degree of fragmentation is reduced. From Figure 5(b) it is obvious that the $C_2H_3^+$ ion has a similar fragmentation pattern as the ions C^+ and CH^+ resulting from a strong fragmentation. This can be seen from its significantly lower production at the 1s → 3s ($\nu_3 = 1$) excitation and the higher production for the 1s → 3p excitation. C^+ and CH^+ are most efficiently produced following an excitation into the 4ℓ, 5ℓ, and 6ℓ Rydberg states. To understand from which photoion the different step II reaction product ions are originating, the distribution of the reaction product ions for the different resonant photon excitations (Figure 5) can be estimated. The ion yield ratios of the distribution for each product ion x are given in Table 3.
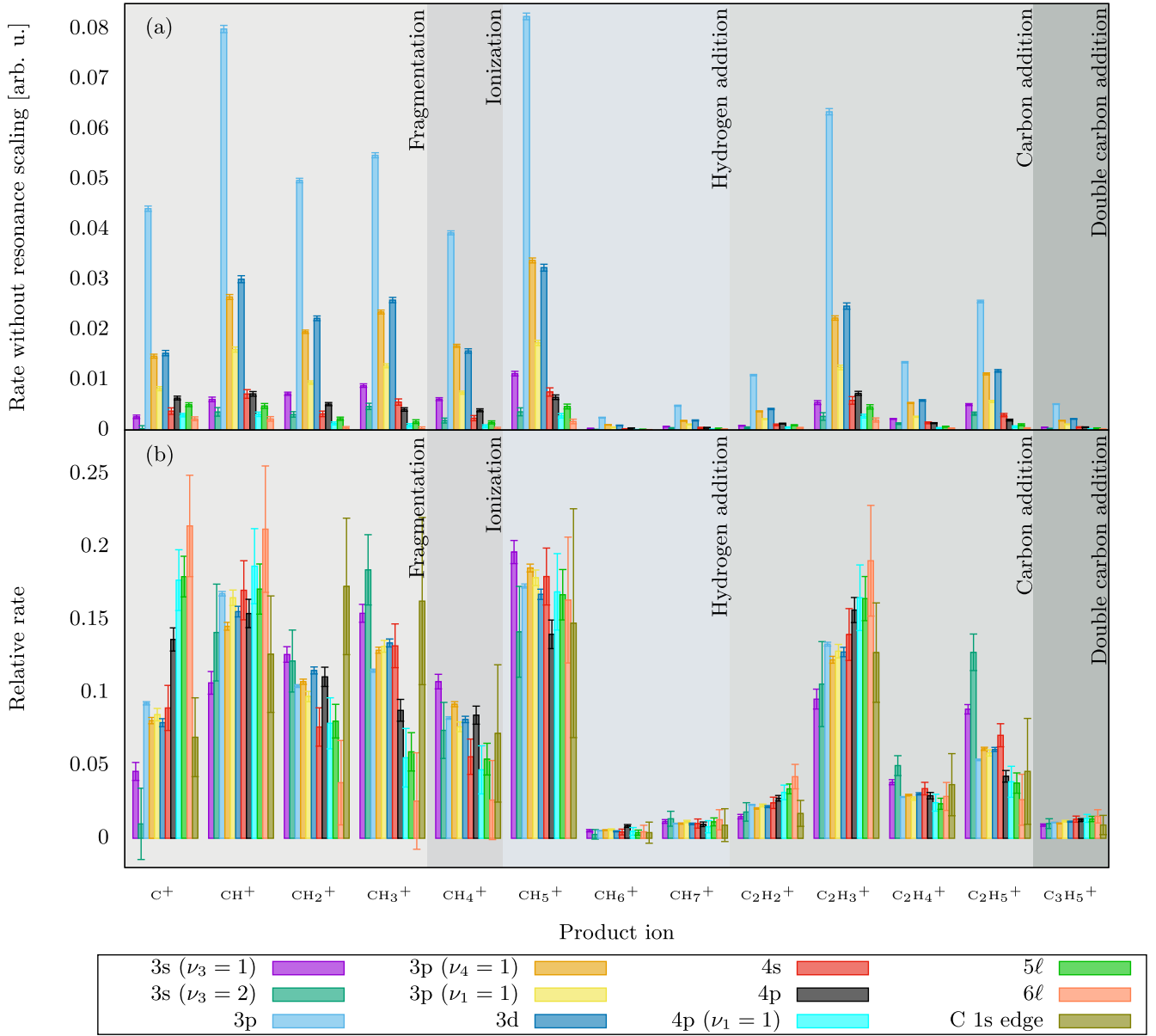
Figure 5. The areas of the individual resonances determined from the Voigt fits in relative units are shown in panel (a). In addition to the simple methane ionization channels, the fragmentation channels and the reaction channels are also shown. To enable a comparison between the resonances, the composition of the channels is shown in panel (b). In order to obtain the composition for each resonance, the sum of the different product ions was set to one for each resonance.

These values are represented by the vectors I_x:

$$I_x = \begin{pmatrix} 3s\ (\nu_3 = 1)_x \\ 3s\ (\nu_3 = 2)_x \\ 3p_x \\ 3p\ (\nu_4 = 1)_x \\ 3p\ (\nu_1 = 1)_x \\ 3d_x \\ 4s_x \\ 4p_x \\ 4p\ (\nu_1 = 1)_x \\ 5\ell_x \\ 6\ell_x \end{pmatrix}. \tag{2}$$

with x being one of the observed product ions (CH_5^+, $C_2H_2^+$, $C_2H_3^+$, $C_2H_4^+$, $C_2H_5^+$). To determine the fraction of the photoions $y = C^+$, CH^+, CH_2^+, CH_3^+, and CH_4^+, the composition of a reaction product ion can be represented as a linear combination of the photoions:

$$I_x = \sum_y a_{x,y} I_y. \tag{3}$$

$a_{x,y}$ designates how the photoion y contributes to the reaction product x. The factors $a_{x,y}$ can be estimated by minimizing the difference $\Delta I_x = I_{x,\mathrm{exp}} - I_x$ between the experimentally found $I_{x,\mathrm{exp}}$ depicted in Figure 5 and the one calculated by Equation (3). The further analysis focuses only on the first step starting the reaction. This gives five reaction products x and five ionic photofragments y. Every reaction product ion x is

characterized by a linear combination of five photoions y. For a reaction product, the difference ΔI_x is given by

$$\Delta I_x = I_{x,\mathrm{exp}} - a_{x,\mathrm{C}^+}I_{\mathrm{C}^+} - a_{x,\mathrm{CH}^+}I_{\mathrm{CH}^+}$$
$$- a_{x,\mathrm{CH}_2^+}I_{\mathrm{CH}_2^+} - a_{x,\mathrm{CH}_3^+}I_{\mathrm{CH}_3^+}$$
$$- a_{x,\mathrm{CH}_4^+}I_{\mathrm{CH}_4^+}. \qquad (4)$$

Here, $a_{x,y}$ is the factor describing the formation of the reaction product x from the photoion y. In order to evaluate the composition of the linear combination with the composition of the reaction product ions, the absolute values of the differences for the individual resonances and reaction products were added up yielding

$$p_{\mathrm{sum}} = ||\Delta I_{\mathrm{CH}_5^+}||_1 + ||\Delta I_{\mathrm{C}_2\mathrm{H}_2^+}||_1 + ||\Delta I_{\mathrm{C}_2\mathrm{H}_3^+}||_1$$
$$+ ||\Delta I_{\mathrm{C}_2\mathrm{H}_4^+}||_1 + ||\Delta I_{\mathrm{C}_2\mathrm{H}_5^+}||_1, \qquad (5)$$

with the taxicab norm summing up the absolute values of the vector components, i.e.,

$$||\boldsymbol{x}||_1 = \sum_{i=0}^{N} |x_i|. \qquad (6)$$

The total sum p_{sum} was used as a measure for the suitability of the description by a linear combination. As a secondary condition, for each photoion y, it was assumed that the sum of the factors $a_{x,y}$ must be less than one. This condition is intended to prevent the modeled photoion yield from exceeding the experimental photoion yield. The function optimize.differential_evolution from the SciPy package (Virtanen et al. 2020) was used to find a solution for the 25 factors $a_{x,y}$ by minimizing the total sum p_{sum}. This function is based on the differential-evolution algorithm (Storn & Price 1997). The solution of this method is shown in Figure 6. The bars represent the factors $a_{x,y}$. From these numbers, we can now specify possible growth reaction pathways for the observed products. Equation (R3) describes the hydrogen-addition reaction to produce the CH_5^+ ion:

$$\mathrm{CH}_4 \xrightarrow[\mathrm{H}_{4-k}^+]{h\nu} [\mathrm{CH}_k^+]^{\neq} \xrightarrow[\mathrm{CH}_{k-1}]{\mathrm{CH}_4} \mathrm{CH}_5^+. \qquad (R3)$$
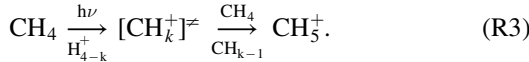
For simplicity, in Equation (R3) for the second elimination only a neutral CH_{k-1} is given. However, the neutral fragment does not necessarily have to be this molecule as further neutral fragmentation pathways such as $\mathrm{CH} + \mathrm{H}$ or $\mathrm{C} + \mathrm{H}_2$ are possible.

From Figure 6 we can conclude that in the experiment k equals 3 or 4 in most cases, i.e., CH_5^+ is formed mainly from CH_3^+ or CH_4^+ photoions. It can be seen from Equation (R3) that a small k means that the neutral by-products should possess very few or even no hydrogen atoms. According to Figure 6 also C^+ and CH^+ should contribute to the formation of CH_5^+. Especially the large C^+ signal is surprising, as it cannot form CH_5^+ by a single collision with CH_4. A possible explanation is a further collision with a second CH_4 molecule, as described by the following equation:

$$\mathrm{C}^+ \xrightarrow[\mathrm{H}]{\mathrm{CH}_4} \mathrm{C}_2\mathrm{H}_3^+ \xrightarrow[\mathrm{C}_2\mathrm{H}_2]{\mathrm{CH}_4} \mathrm{CH}_5^+. \qquad (R4)$$
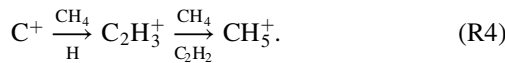
Such more complex, multistep reactions of highly reactive product ions, e.g., $\mathrm{C}_2\mathrm{H}_3^+$, are not included in our model and show its limitation. Furthermore, the CH_5^+ ion yield in Figure 5(b) shows almost no variation between the resonances and this might limit the precision of the optimization algorithm
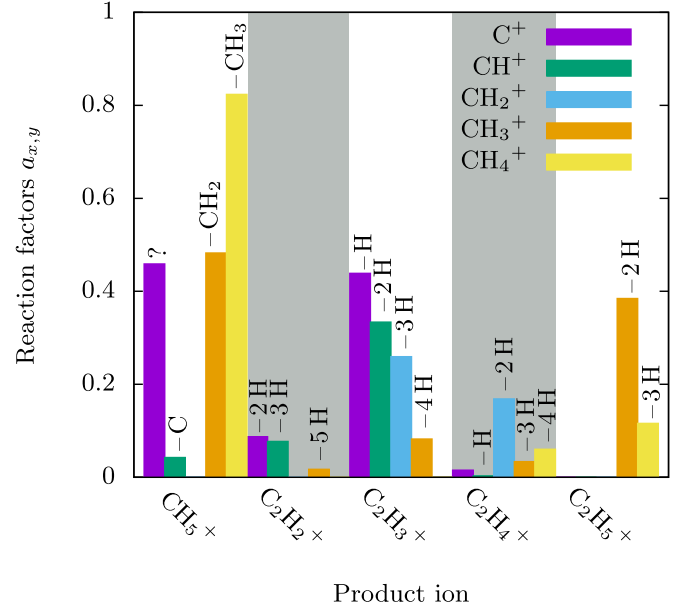
Figure 6. Reaction factors $a_{x,y}$ as obtained from the linear combination model (Equations (4) and (5)). The neutral elimination products resulting from the ion–methane reaction are written on the respective bars. Since for CH_5^+ the differences between the resonances are very small, the algorithm assumes a mixture of different ions. This is a weak point of the linear combination model. CH_5^+ cannot originate from a reaction between C^+ and a methane molecule. For this reason we put a question mark on the respective bar (for further discussion see text). The uncertainties of the individual contributions represented by the bars are around 10%.

for CH_5^+. The $\mathrm{C}_2\mathrm{H}_2^+$ ion is formed mostly from C^+ or CH^+. Since the $\mathrm{C}_2\mathrm{H}_2^+$ ion has only two hydrogen atoms it is advantageous that it is formed by an ion with one or none hydrogen atoms. In this way, only two or three hydrogen atoms have to be eliminated during the reaction.

For the most frequent product $\mathrm{C}_2\mathrm{H}_3^+$, the situation becomes more complicated as in addition to C^+ and CH^+ also CH_2^+ and CH_3^+ are involved in the formation process. For $\mathrm{C}_2\mathrm{H}_4^+$, the trend continues with the involvement of reactants with more hydrogen atoms. The C^+ and CH^+ contributions are already significantly lower in the formation of $\mathrm{C}_2\mathrm{H}_4^+$ as compared to $\mathrm{C}_2\mathrm{H}_3^+$. To produce a $\mathrm{C}_2\mathrm{H}_4^+$ ion from C^+ ions within a single collision, no H can be eliminated. Due to momentum conservation, this process becomes very unlikely, resulting in a very small C^+ contribution. The residual C^+ contribution to the $\mathrm{C}_2\mathrm{H}_4^+$ product can be taken as an indication of the limited accuracy of our analysis.

For the reaction $\mathrm{CH}^+ + \mathrm{CH}_4 \rightarrow \mathrm{C}_2\mathrm{H}_4^+ + \mathrm{H}$, there should be a single hydrogen-atom elimination, but this reaction is found to be very weak in our analysis.

The reaction from CH_2^+ to $\mathrm{C}_2\mathrm{H}_4^+$ can take place with an elimination of two H atoms or one H_2 molecule. It has the highest probability to form $\mathrm{C}_2\mathrm{H}_4^+$, which can be directly seen in Figure 6. The result for the $\mathrm{C}_2\mathrm{H}_5^+$ product ion is very similar. The product is formed exclusively from CH_3^+ and CH_4^+. The formation of $\mathrm{C}_2\mathrm{H}_5^+$ from the collision of a CH_2^+ ion with CH_4 is not found. This would correspond to an elimination of an H atom. This H elimination seems to be unlikely for the larger $\mathrm{C}_2\mathrm{H}_x^+$ ions, as this reaction is not found for the $\mathrm{C}_2\mathrm{H}_4^+$ and $\mathrm{C}_2\mathrm{H}_5^+$ product ions. Here, we can conclude that the elimination of two H atoms or an H_2 molecule is favored.

Table 4
References to the Identification of Hydrocarbon Ions in Different Environments and Experiments

Products	UV Experiments	Titan Atmosphere		Other Atmosphere		Interstellar Medium	
		Neutral	Ion	Neutral	Ion	Neutral	Ion
C^+	...	...	✓[a]	✓[b]	...	✓[c]	...
CH^+	...	...	✓[a]	...	...	✓[c]	✓[c,d]
CH_2^+	✓[e]	...	✓[a]	...	...	✓[f]	...
CH_3^+	✓[e,g]	...	✓[a]	✓[b]	...	...	...
CH_4^+	✓[e,g]	✓[h,i]	✓[a]	✓[b,i]	...	...	...
CH_5^+	✓[e,g]	...	✓[a]	...	...	...	...
CH_6^+	...	...	✓[a]	...	...	...	...
CH_7^+	...	...	✓[a]	...	...	...	...
C_2H^+	...	...	...	...	...	✓[j]	...
$C_2H_2^+$	...	✓[h,k]	✓[a]	✓[b,l]	...	...	...
$C_2H_3^+$	...	...	✓[a]	...	...	...	...
$C_2H_4^+$	✓[e,k]	✓[h]	✓[a]	✓[b,l]	...	...	...
$C_2H_5^+$	✓[e,g]	...	✓[a]	...	...	...	...
$C_2H_6^+$	...	✓[h,k]	✓[a]	✓[b,l]	...	...	...
$C_3H_3^+$	...	✓(C_3H_2)[m]	✓[a]	...	...	✓[n]	...
$C_3H_4^+$	...	✓[k]	✓[a]	✓[b]	...	✓[o]	...
$C_2H_5^+$	...	...	✓[a]	...	...	...	...

Notes. The first column provides a list of molecular ions that were found in the present X-ray absorption experiment. The second column shows which ions have already been found in similar UV experiments. The third and fourth column shows the neutral and ionic molecules, respectively, that have already been found in Titan's atmosphere. The fifth and sixth columns show the same for other atmospheres and the seventh and eighth for the interstellar medium.
[a] Cravens et al. (2006).
[b] Atreya et al. (2003).
[c] Habart et al. (2010).
[d] Naylor et al. (2010).
[e] Thissen et al. (2009).
[f] Hollis et al. (1995).
[g] Bourgalais et al. (2019).
[h] Gillett (1975); Vuitton et al. (2006).
[i] Kuiper (1944).
[j] Mccarthy et al. (1995).
[k] Hanel et al. (1981).
[l] Yelle et al. (1993).
[m] Nixon et al. (2020).
[n] Tanaka et al. (1997).
[o] Churchwell & Hollis (1983); Cazzoli & Puzzarini (2008).

5. Conclusion

By using the ion trap of the PIPE setup implemented in the soft X-ray beamline P04 at the synchrotron light source PETRA III and an ion time-of-flight spectrometer, the production of small hydrocarbon ions following a resonant C 1s excitation in methane, CH_4, molecules have been investigated. Besides the expected photofragments CH_n^+ ($n = 0$–4), hydrocarbon cations larger than methane ranging from CH_5^+, and the supermethanium ions CH_6^+ and CH_7^+ all the way to $C_3H_5^+$ have been found. The photon-energy-dependent production largely follows the methane C 1s excitation resonances. However, also distinct differences are found, which are attributed to the different fragmentation pathways that follow after photoabsorption by neutral methane populating different intermediate core-excited vibrational states. The production of heavier hydrocarbon molecules can be explained by chain growth due to collisions of the trapped ionic photofragments with neutral methane. In contrast to former studies using VUV radiation (Thissen et al. 2009; Peng et al. 2013; Bourgalais et al. 2019), soft X-ray radiation is efficiently creating the small photofragments C^+, CH^+, and CH_2^+ (Wolff et al. 2012). This results in the production of highly reactive hydrocarbon ions such as $C_2H_2^+$ and $C_2H_3^+$ with a small number of hydrogen atoms, which have not been unambiguously identified in former studies using VUV radiation.

Due to the rather low solar photon flux of soft X-rays, two to three orders below the VUV photon flux, soft X-rays have not been taken into account in previous studies of chemical compositions of planetary atmospheres. However, due to the higher degree of fragmentation by soft X-rays and due to the enhanced C 1s resonant cross section, the probability of producing highly reactive species with a small number of hydrogen atoms is strongly enhanced and might thereby efficiently influence the chemistry in planetary atmospheres and the interstellar medium. As in the present experiments, the masses 26 u, 27 u, and 28 u, corresponding to $C_2H_2^+$, $C_2H_3^+$, and $C_2H_4^+$ were discovered in the ionosphere of Titan (see Table 4) during the Cassini mission.

Our results indicate that soft X-rays play an important role in molecular growth processes occurring in planetary atmospheres and should be taken into account. Compared to CH_4/N_2 mixtures only a single collision is required to form highly reactive ions, which might further enhance the probability of

further carbon-adding reactions. The ions resulting from the first reaction can react in a further step to $C_3H_3^+$, $C_3H_4^+$, and $C_3H_5^+$ and might eventually form heavier hydrocarbon molecules such as C_6H_6.

Furthermore, the masses of the supermethanium ions 18 u (CH_6^+) and 19 u (CH_7^+) coincide with the masses of water, hydronium, and the ammonium ion NH_4^+, which have been observed in the mass spectra of the ionosphere of Titan. Since the mass of water is present to a greater extent than previously assumed in the models (Cravens et al. 2006), it could be that a part of the mass 18 u peak is due to the supermethanium ion CH_6^+. The composition of the mass peaks recorded in the ionosphere of Titan cannot be explained by a simple few-component mass spectrum.

In summary, we have shown that soft X-rays could well play an important role in the formation of small hydrocarbon systems in planetary atmospheres due to the large cross sections and the high degree of fragmentation. It might be necessary to include them in corresponding models for the formation of larger molecules. By applying the presented method even larger hydrocarbon ions might be generated by soft X-rays when starting with larger molecular species.

Acknowledgments

ORCID iDs

S. Reinwardt ® https://orcid.org/0000-0001-8106-7124
I. Baev ® https://orcid.org/0000-0003-0714-9070
P. Cieslik ® https://orcid.org/0000-0002-4702-5251
K. Baev ® https://orcid.org/0000-0002-0146-6318
T. Buhr ® https://orcid.org/0000-0003-3337-1740
A. Perry-Sassmannshausen ® https://orcid.org/0000-0002-0700-3875
S. Schippers ® https://orcid.org/0000-0002-6166-7138
A. Müller ® https://orcid.org/0000-0002-0030-6929
F. Trinter ® https://orcid.org/0000-0002-0891-9180
J. Viefhaus ® https://orcid.org/0000-0003-1154-0750
M. Martins ® https://orcid.org/0000-0002-1228-5029

References

Atreya, S. K., Mahaffy, P. R., Niemann, H. B., Wong, M. H., & Owen, T. C. 2003, P&SS, 51, 105
Bagus, P. S., Krauss, M., & LaVilla, R. E. 1973, CPL, 23, 13
Banaszkiewicz, M., Lara, L. M., Rodrigo, R., López-Moreno, J. J., & Molina-Cuberos, G. J. 2000, Icar, 147, 386
Bartmess, J. E., & Georgiadis, R. M. 1983, Vacuu, 33, 149
Bastian, B., Michaelsen, T., Meyer, J., & Wester, R. 2019, ApJ, 878, 162
Berné, O., & Tielens, A. G. G. M. 2011, PNAS, 109, 401
Bhardwaj, A., Elsner, R. F., Waite, J. H., et al. 2005, ApJL, 624, L121
Bourgalais, J., Carrasco, N., Vettier, L., & Pernot, P. 2019, JGRA, 124, 9214
Branduardi-Raymont, G., Bhardwaj, A., Elsner, R. F., & Rodriguez, P. 2010, A&A, 510, A73
Buck, J., Bagschik, K., Glaser, L., et al. 2019, AIP Conf. Proc., 2054, 060057
Caspi, A., Woods, T. N., & Warren, H. P. 2015, ApJL, 802, L2
Cazzoli, G., & Puzzarini, C. 2008, A&A, 487, 1197
Churchwell, E., & Hollis, J. M. 1983, ApJ, 272, 591
Cravens, T. E., Robertson, I. P., Waite, J. H., Jr, et al. 2006, GeoRL, 33, L07105
Fox, J. L., & Yelle, R. V. 1997, GeoRL, 24, 2179
Fulchignoni, M., Ferri, F., Angrilli, F., et al. 2005, Natur, 438, 785
Gerlich, D. 1992, in Inhomogeneous RF Fields: A Versatile Tool for the Study of Processes with Slow Ions (Advances in Chemical Physics) Vol. 82ed. C.-Y. Ng et al. (Hoboken, NJ: Wiley),
Gerlich, D. 2005, PCCP, 7, 1583
Gillett, F. C. 1975, ApJL, 201, L41
Gioumousis, G., & Stevenson, D. P. 1958, JChPh, 29, 294
Gussoni, M., Rui, M., & Zerbi, G. 1998, JMoSt, 447, 163
Habart, E., Dartois, E., Abergel, A., et al. 2010, A&A, 518, L116
Hanel, R., Conrath, B., Flasar, F. M., et al. 1981, Sci, 212, 192
Heck, A. J. R., Zare, R. N., & Chandler, D. W. 1996, JChPh, 104, 4019
Herbst, E., & Klemperer, W. 1973, ApJ, 185, 505
Hollenbach, D. J., & Tielens, A. G. G. M. 1999, RvMP, 71, 173
Hollis, J. M., Jewell, P. R., & Lovas, F. J. 1995, ApJ, 438, 259
Holmes, N. S. 2007, AtmEn, 41, 2183
Hörst, S. M. 2017, JGRE, 122, 432
Keller, C. N., Anicich, V. G., & Cravens, T. E. 1998, P&SS, 46, 1157
Kuiper, G. P. 1944, ApJ, 100, 378
Kulmala, M. 2003, Sci, 302, 1000
Langevin, M. P. 1905, AnCPh, 8, 245
Lemus, R., & Frank, A. 1994, JChPh, 101, 8321
Mccarthy, M. C., Gottlieb, C. A., & Thaddeus, P. 1995, JMoSp, 173, 303
McGuire, B. A. 2022, ApJS, 259, 30
Meyer, J., & Wester, R. 2017, ARPC, 68, 333
Mikosch, J., Frühling, U., Trippel, S., et al. 2008, PhRvA, 78, 023402
Müller, A., Borovik, A., Jr, Buhr, T., et al. 2018, PhRvA, 97, 013409
Naylor, D. A., Dartois, E., Habart, E., et al. 2010, A&A, 518, L117
Nixon, C. A., Thelen, A. E., Cordiner, M. A., et al. 2020, AJ, 160, 205
Martinez, J. O., Jr, Betts, N. B., Villano, S. M., et al. 2008, ApJ, 686, 1486
Peng, Z., Gautier, T., Carrasco, N., et al. 2013, JGRE, 118, 778
Reinwardt, S., Baev, I., Linß, F., et al. 2023, RScI, 94, 023201
Rusov, V. D., Sharph, I. V., Smolyar, V. P., Eingorn, M. V., & Beglaryan, M. E. 2021, PDU, 31, 100746
Schirmer, J., Trofimov, A. B., Randall, K. J., et al. 1993, PhRvA, 47, 1136
Senkan, S., & Castaldi, M. 1996, CoFl, 107, 141
Sharma, A. K., & Yasuda, H. 1989, J. Appl. Polym. Sci., 38, 741
Storn, R., & Price, K. 1997, J. Global. Optim., 11, 341
Tanaka, K., Sumiyoshi, Y., Ohshima, Y., Endo, Y., & Kawaguchi, K. 1997, JChPh, 107, 2728
Thissen, R., Vuitton, V., Lavvas, P., et al. 2009, JPCA, 113, 11211
Tielens, A. G. G. M. 2008, ARA&A, 46, 289
Urquhart, S. G., & Gillies, R. 2005, JPCA, 109, 2151
Virtanen, P., Gommers, R., Oliphant, T. E., et al. 2020, NatMe, 17, 261
Vuitton, V., Yelle, R.V., & Lavvas, P. 2008a, RSPTA, 367, 729
Vuitton, V., Yelle, R. V., & Anicich, V. G. 2006, ApJL, 647, L175
Vuitton, V., Yelle, R. V., & Cui, J. 2008b, JGR, 113, E05007
Waite, J. H., Young, D. T., Cravens, T. E., et al. 2007, Sci, 316, 870
Wei, B., Chen, Z., Wang, X., et al. 2013, JPhB, 46, 215205
Wexler, S., & Jesse, N. 1962, JACS, 84, 3425
Wolff, W., Sigaud, L., Montenegro, E. C., et al. 2012, JPCA, 117, 56
Woods, T. N., Bailey, S., Eparvier, F., et al. 2000, PCEC, 25, 393
Yelle, R. V., Herbert, F., Sandel, B. R., Vervack, R. J., Jr, & Wentzel, T. M. 1993, Icar, 104, 38
Young, P. R. 2021, FrASS, 8, 50